Formation and coarsening of Ag(110) bilayer islands on NiAl(110): STM analysis and atomistic lattice-gas modeling

Yong Han,[1,*] Barış Ünal,[2,3,†] Dapeng Jing,[4,3] Feili Qin,[1,3] C. J. Jenks,[3] Da-Jiang Liu,[3] P. A. Thiel,[4,2,3] and J. W. Evans[5,6,3]
[1]*Institute of Physical Research and Technology, Iowa State University, Ames, Iowa 50011, USA*
[2]*Department of Materials Science and Engineering, Iowa State University, Ames, Iowa 50011, USA*
[3]*Ames Laboratory, U.S. DOE, Iowa State University, Ames, Iowa 50011, USA*
[4]*Department of Chemistry, Iowa State University, Ames, Iowa 50011, USA*
[5]*Department of Physics and Astronomy, Iowa State University, Ames, Iowa 50011, USA*
[6]*Department of Mathematics, Iowa State University, Ames, Iowa 50011, USA*
(Received 21 July 2009; revised manuscript received 31 December 2009; published 31 March 2010)

Scanning tunneling microscopy analysis of the initial stages of film growth during deposition of Ag on NiAl(110) reveals facile formation of bilayer Ag(110) islands at temperatures of 130 K and above. Annealing subsequent to deposition at 130 K induces coarsening of the bilayer island distribution. The thermodynamic driving force for bilayer island formation reflects a lower relative surface energy for films of even layer thicknesses. This feature derives from quantum size effects due to electron confinement in the Ag film. The kinetics of island formation and relaxation is controlled by terrace and edge-diffusion barriers, detachment barriers, interlayer diffusion barriers, and layer-dependent adsorption and interaction energies. These key energies are determined from density-functional theory analysis and incorporated into an atomistic lattice-gas model for homogeneous island formation, where specification of the adatom hop rates is consistent with detailed balance. Model analysis via kinetic Monte Carlo simulation elucidates the role of strongly anisotropic interactions in development during deposition of elongated island growth shapes and also in facilitating upward mass transport needed for bilayer island formation. The model succeeds in recovering island densities at lower temperatures but experimental densities exceed model predictions at higher temperatures plausibly due to heterogeneous nucleation at surface defects. The same model successfully describes postdeposition coarsening of small islands grown at 130 K.

DOI: 10.1103/PhysRevB.81.115462 PACS number(s): 68.55.−a, 68.35.Ja, 68.35.Md, 68.37.Ef

I. INTRODUCTION

Traditionally, epitaxial film growth has been classified into three "quasiequilibrium" growth modes.[1] Frank-van der Merwe (FM) growth, i.e., layer-by-layer growth, typically occurs for overlayers with low surface free energy relative to the substrate and with low strain. In contrast, often three-dimensional (3D) islands form either during the initial stages of heteroepitaxy for Volmer-Weber growth or after development of a wetting layer for Stranski-Krastanov growth. Such 3D islands are expected for high surface-energy adsorbates. They are also expected for high interface energies often associated with the buildup of strain in the growing film.

However, growth modes quite different from those above are sometimes observed for metal-on-metal film growth. These include sandwichlike growth where atoms from a low surface-energy substrate climb on top of the overlayer.[2–4] Other possibilities of more relevance in this study include the development of bilayer islands on single-element metal substrates[4–8] and on alloy substrates.[9–11] The development of flat-topped or mesalike multilayer islands has also been observed on single-element metal substrates[12–16] and on alloys.[17,18] Formation of such morphologies can occur even for metal adsorbates with low surface energies such as Ag and Pb where one might expect FM growth.

The thermodynamic driving force for growth of height-selected, mesalike multilayer metal islands is often associated with quantum size effects (QSE): electron confinement within the film produces a height-dependent surface free energy so that islands with different thicknesses have different thermodynamic stabilities. Furthermore, oscillatory thermodynamic stability of a metal film upon varying thickness reflects a matching condition: the half Fermi wavelength $\lambda_F/2$ should be commensurate with the film thickness which is some multiple of the interlayer spacing d.[19–21] For a Ag(110) film, $d=0.1439$ nm and $\lambda_F=0.5206$ nm at zero temperature (0 K).[21] Thus, $\lambda_F/2$ corresponds to 90% of a bilayer film thickness of $2d$. This indicates that Ag(110) films should display a primary stability oscillation with a period of two layers, in agreement with the density-functional theory (DFT) energetics.[20,21]

Formation of bilayer islands could reflect QSE. However, it is also possible that their formation primarily reflects stronger adatom adsorption and/or interaction on top of a monolayer and thicker films relative to the substrate, together with kinetic inhibition of the nucleation of 3rd and higher layers. Note also that since bilayer and 3D multilayer island formation involve upward mass transport, these processes are likely to be kinetically hindered at lower temperatures. In fact, there is little detailed analysis of the kinetics in these systems. Experimental examples where bilayer formation is inhibited (but assisted by substrate steps) exist for Fe on Ag(100),[14] and Co on Cu(111).[7] Some modeling of kinetics exists for the formation of bilayer Co islands on Cu(100),[22] and multilayer Pb islands on Si(111).[23–26] Our goal here for the Ag/NiAl(110) system is to develop a detailed and realistic atomistic model to describe the complete island formation process, thereby elucidating the facile formation of bilayer islands even at low temperatures.

There is also interest in postdeposition stability versus coarsening of distributions of separated islands. There have been extensive studies of coarsening and decay for 3D islands in heteroepitaxial systems,[27] and more recently for 2D islands in homoepitaxial systems.[28,29] In these systems, the thermodynamic driving force for coarsening is a reduction in the free energy associated with island periphery, so evolution is just driven by differences in effective island radii. The presence of QSE (Ref. 30) or partial bilayer island formation could produce distinct behavior. Thus, we are interested in quantifying coarsening in the Ag/NiAl(110) system and in assessing whether behavior is also captured by the above mentioned atomistic model.

In this paper, we analyze both the formation and coarsening of bilayer Ag islands on NiAl(110). In Sec. II, we briefly summarize key experimental procedures and observations, as well as describing computational procedures for our DFT calculations of energetics. Then, in Sec. III, our scanning tunneling microscopy (STM) observations are presented for the nucleation and growth of bilayer Ag islands on NiAl(110) for deposition at 130 K and above. In addition, we analyze postdeposition coarsening (during annealing) of small bilayer islands formed at 130 K. DFT results for supported Ag films are presented in Sec. IV for adsorption energies (reflecting QSE), interaction energies, and key diffusion barriers. In Sec. V, our atomistic model is described for this system which incorporates the above DFT energetics. We present results from kinetic Monte Carlo (KMC) simulations in Sec. VI. The model is shown to successfully describe not just facile bilayer island formation at low T but also postdeposition coarsening. Section VII provides further discussion and summarizes our findings.

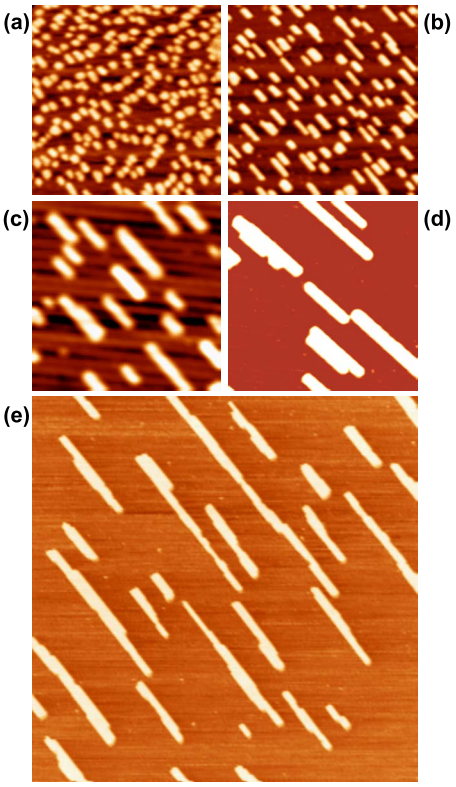

FIG. 1. (Color online) STM images of Ag bilayer islands formed on NiAl(110) surface by Ag deposition with flux $F=3.3\times10^{-3}$ BL/s at (a) 127 K, (b) 140 K, (c) 190 K, (d) 250 K, and (e) 300 K. Image sizes are 72.5×72.5 nm^2 for (a)–(d) and 500×500 nm^2 for (e). Note that the [001] crystallographic direction of the NiAl(110) substrate is in the direction of elongation of the Ag islands.

II. EXPERIMENTAL DETAILS, COMPUTATIONAL METHODS, AND ISLAND STRUCTURE

Details of our vacuum chamber setup, NiAl sample preparation, Ag deposition procedure, and STM analysis are described in Refs. 10 and 11. STM images reveal that our sample preparation procedures can produce a NiAl(110) surface with broad terraces up to 1 μm wide. Thus, all images shown are for a single substrate terrace (although different terraces are imaged for growth studies at different T). The substrate crystallographic direction is described in the captions of Figs. 1 and 2, but for all subsequent STM and KMC images, the [001] direction is always in the vertical direction on the page. In our studies of island formation, we typically deposit about 0.4 monolayers (MLs) or 0.2 bilayers (BLs) of Ag on NiAl(110) at an estimated flux of $F=3.3\times10^{-3}$ BL/s. One bilayer is defined as two monolayers of a perfect Ag(110) film.

DFT calculations are performed using the plane-wave-based Vienna *ab initio* simulation package (VASP).[31] We use the Perdew-Burke-Ernzerhof form of the generalized gradient approximation.[32] The electron-ion interactions are described by the projector augmented-wave approach.[33] The converged magnitude of the forces on all relaxed atoms is always less than 0.1 eV/nm. To prevent spurious interactions between adjacent replicas of the thin-film system, we use a vacuum layer that is 15 Å thick in the direction perpendicular to the surface. The optimized lattice constants are $a_{\mathrm{Ag}}=0.4166$ nm for Ag, and $a_{\mathrm{NiAl}}=0.2896$ nm for NiAl, to be compared with the experimental values 0.4086 nm and 0.2887 nm, respectively. Diffusion paths and barriers are determined via the climbing nudged elastic band (cNEB) method.[34] These DFT energetics will be incorporated into an atomistic lattice-gas model for epitaxial growth of Ag(110) films described in Sec. V. Model behavior is analyzed by KMC simulation.

In our model development, we assume that Ag islands on NiAl(110) have an fcc(110) structure (see Appendix A), and will find a preference to form bilayer rather than monolayer islands. One factor favoring such epitaxial growth is the almost perfect match between the surface unit cells for NiAl(110) and Ag(110).[10,11] This feature would also preclude lateral mismatch strain as a source of the deviation from monolayer island growth. Evidence supporting the fcc(110) bilayer structure came from agreement between the experimentally measured height of 0.32 nm and DFT results.[10] Furthermore, a slight periodic ripple in the height of islands was also seen in DFT analysis of relaxed fcc(110) bilayer structures.[10] Deviation from fcc(110) bilayer-by-bilayer growth is observed for much thicker films, as seen in other Ag heteroepitaxy systems due to a preference for the lower

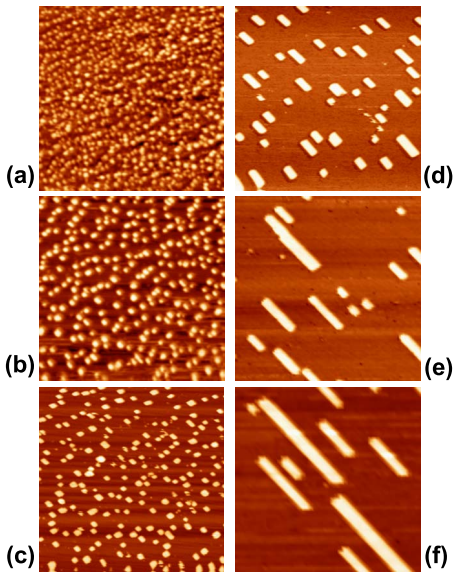

FIG. 2. (Color online) STM images of Ag bilayer island coarsening following formation by Ag deposition on NiAl(110) surface at 130 K with flux $F=2.8\times10^{-2}$ BL/s. The time after deposition at the corresponding temperature is (a) 0 min at 130 K, (b) 67 min at 175 K, (c) 100 min at 197 K, (d) 162 min at 234 K, (e) 203 min at 252 K, and (f) 277 min at 274 K, respectively. The size of any image is 100×100 nm^2. Note that the [001] crystallographic direction of the NiAl(110) substrate is in the direction of elongation of the Ag islands.

surface-energy Ag(111) structure. However, this behavior is not relevant for the initial stages of growth considered here.

Next, additional evidence for the bilayer fcc(110) island structure is discussed. Using DFT, we have searched for and found alternative low-energy film structures (described in Appendix A as double chain and square hex). However, none of the stable monolayer or multilayer versions of these structures is close to matching the experimentally observed island height.

Finally, there is also compelling experimental evidence from low-energy electron diffraction (LEED) analysis. We have compared the LEED pattern for the clean substrate with that for a 3.0 ML film deposited at 300 K (for which the substrate is completely covered by a Ag film of thickness 0.32 nm and 50% of that film is covered by rectangular Ag islands with step height 0.29 nm). One observes essentially identical rectangular arrangements of diffraction spots for both the clean substrate and the 3.0 ML film for all electron energies examined between 100 and 250 eV. The aspect ratio of the rectangular Brillouin zone is 1.415 in both cases and the reciprocal space dimensions agree to within 0.4%. It should be emphasized that for these energies, the mean-free path for electrons in Ag is short, as low as 0.65 nm and no higher than 0.8 nm.[35] Thus, essentially all of the LEED intensity comes from diffraction from the Ag film, not the substrate, so the above observations provide compelling evidence for the fcc(110) structure of the Ag film. We also note that upon varying the electron energy, adjacent spots display out-of-phase oscillation, also as expected for a fcc structure.[36,37]

III. STM ANALYSIS OF BILAYER ISLAND EVOLUTION

Figure 1 shows rectangular islands formed by depositing ~0.2 BL of Ag on NiAl(110) at temperatures between $T=127$ and 300 K with $F=3.3\times10^{-3}$ BL/s. Their height is always 0.32 nm, a value consistent with a Ag(110) bilayer structure. Island densities $N_{\rm isl}$ are shown in Table I for various T.

If an island density is determined from images containing a total of M islands, then there is an uncertainty in density associated with finite sample size. This follows from the uncertainty (standard deviation), δM, in the number of islands, where $(\delta M)^2\approx CM$, an expression based on exact fluctuation-correlation relations[38,39] which relate C to island pair correlations. Our simulations indicate that $C\approx1/2$ for lower T, although one might conservatively choose $C\approx2-4$, say, to account for the effects of possible heterogeneity of the substrate. Thus, in Table I, we also report the total number, M, of islands counted at each T allowing determination of the percentage uncertainty in the island density from $100(C/M)^{1/2}$. However, there is another source of uncertainty associated with our percolation-type definition of islands (used in the simulations), wherein two barely connected islands should be counted as one. From the STM images, it is not clear whether islands are connected particularly for higher densities of smaller islands. This introduces an additional uncertainty of perhaps ±10% at 127 K but significantly lower at higher T.

The variation in island density with T is described for lower T by $N_{\rm isl}\propto e^{-\beta E}$ with an Arrhenius energy of $E=0.08-0.09$ eV. Here, $\beta\equiv1/(k_BT)$, and k_B is the Boltzmann constant. This behavior might be interpreted by a traditional mean-field rate equation (RE) analysis[38,40] assuming effectively irreversible homogeneous nucleation and growth of islands (i.e., critical size $i=1$) with near-isotropic terrace diffusion (which we will show is appropriate here). Then, the observed Arrhenius behavior implies an isotropic diffusion barrier of $E_d=3E=0.24-0.27$ eV for Ag on NiAl(110). However, this treatment is overly simplistic.

TABLE I. Experimental Ag island density $N_{\rm isl}$ (in units of 10^{-3} nm^{-2}) versus deposition temperature T (in units of K). The number, M, of islands counted at each T is also shown. Adsorption site (unit cell) area is 0.118 nm^2. Note that we use more data than that in our previous analysis (Ref. 11) resulting in slightly different values for $N_{\rm isl}$.

T	127	140	150	175	190	225	250	275	300
$N_{\rm isl}$	35	18.0	12.6	4.67	3.49	1.27	0.66	0.21	0.079
M	1620	770	910	480	1530	710	490	320	400

To scrutinize the above nucleation analysis, one can utilize previous simulation results for irreversible formation of compact islands with isotropic diffusion.[38,41] Using $E_d = 0.27$ eV, a prefactor of $\nu = 10^{13}/\mathrm{s}$ and the experimental F yields $N_{\mathrm{isl}} = 4.1 \times 10^{-2}$ nm^{-2} at 140 K compared with 1.8×10^{-2} nm^{-2} from experiment. This discrepancy (neglected previously[11]) reflects some reversibility in island formation at 140 K. This is confirmed by analysis of the "crossover variable"[38,42]

$$Y = \frac{\nu}{F} e^{-\beta(E_d + 1.5E_b)}, \tag{1}$$

where ν is the attempt frequency, E_d is the diffusion barrier (as above), and E_b is the bond strength controlling dimer stability. Y reflects the ratio of dimer dissociation to island growth rates and Y exceeding ~ 10 corresponds to reversible island formation. From this analysis, one concludes that island formation is reversible at 140 K for $E_b < 0.1$ eV which we show applies in this system.

Another complication for this system is that the decrease in island density with increasing T up to 300 K is significantly slower than would be expected given the onset of reversibility below 150 K. Note however that the substrate is a binary alloy surface which in general will display some deviation of near surface from bulk composition leading to point defects associated with substitutional exchange or replacement. Indeed, point defects have been observed by STM on the NiAl(110) surface in our own work and that of other groups.[43,44] They were associated with replacement of Al with Ni to create a Ni-rich surface and with subsurface interstitials. All groups report that these defects are visible for stronger bias conditions but not for lower bias where STM images show surface states as waves. Point defects present similar STM images on other binary alloy surfaces.[45] More complex extended defects such as dislocations and antiphase boundaries were also observed on NiAl(110) surfaces and proposed to play a key role in Al film growth at high T.[46]

Suppose that the above point or extended defects form "strong traps" for nucleation. Then, if the effective defect density is low relative to the density of homogeneously nucleated Ag islands at around 140 K, these defects should not significantly affect island formation at lower T. However, they could impact behavior for higher T. Specifically, an increasing fraction of islands could be nucleated at defect traps for higher T, boosting island density above that for homogeneous nucleation. See Appendices B and C for further analysis. As an aside, another possibility is that buried extended defects might cause "slight perturbations" of the potential-energy surface (PES) seen by diffusing adatoms. These perturbations may not have a significant effect at high T but could impact homogeneous nucleation at low T.

As noted above, the Ag bilayer islands formed during deposition on NiAl(110) have rectangular shapes which are elongated in the [001] crystallographic direction of the NiAl(110) substrate. Furthermore, the aspect ratio of the islands increases with increasing deposition temperature for the entire range probed in these experiments (up to 300 K). In contrast, for Ag/Ag(110) homoepitaxy,[38] one finds that rectangular single-layer high islands form during deposition. Their aspect ratio increases with increasing deposition temperature up to about 200 K but then decreases strongly for temperatures around 220–250 K (depending on F). Presumably the bilayer structure of Ag islands on NiAl(110) "locks in" the nonequilibrium growth shapes. In contrast, the monolayer islands on Ag(110) are much more dynamic (as confirmed by our simulation studies described below), and thus able to achieve their equilibrium shapes below 300 K.

As an aside, it is appropriate to mention that atomic chains of noble metals (Au, Ag) have been assembled on the NiAl(110) substrate using the STM tip following deposition at very low T.[47–49] Typically, these chains are oriented in the [001] direction which is the natural elongation direction of our self-assembled islands. The correspondence of the separation of adjacent atoms in a chain of this orientation with that in the bulk was presumed to facilitate chain formation.[47] It is however also possible to assemble chains in the orthogonal direction.[48] Rather than troughs on the surface,[49] we would argue that stronger interactions between adatoms aid assembly and stabilization of [001]-oriented chains.

Finally, our analysis of the coarsening of bilayer Ag island distributions is described. Since bilayer islands are relatively stable (cf. above), we enhance the propensity for coarsening in two ways. *First*, we deposit Ag at low $T = 130$ K and with "high" $F = 2.8 \times 10^{-2}$ BL/s to increase the density of islands and thus to reduce their mean size (for fixed coverage). The smaller size implies higher effective curvature of island edges and a higher spread of curvatures, thus producing a stronger driving force for coarsening. In addition, deposition for sufficiently low T and high F could lead to formation of monolayer or incomplete bilayer islands, which should be more susceptible to coarsening. *Second*, we ramp up the temperature after deposition (cf. Fig. 2) in order to enhance the thermally activated coarsening process.

Results shown in Fig. 2 do indeed reveal significant coarsening already when the temperature has climbed to 175 K and extensive coarsening above 200 K. Island shapes become rectangular with increasing aspect ratio above 200 K. This presumably reflects a transition from low-T growth shapes towards higher-T equilibrium shapes. These quasi-equilibrium shapes are not as elongated as the growth shapes from direct deposition at around 300 K.

IV. DFT ANALYSIS OF KEY ENERGETICS

A. Interaction energies

The dependence on thickness L (measured in layers), of the average energy per Ag atom in the supported Ag(110) film, E_L^{Ag}, controls the thermodynamic "growth" mode. However, to elucidate nonequilibrium growth behavior, we consider additional quantities including the L dependence of the adsorption energy of an isolated Ag adatom, E_L^{ads}, upon a film of $L-1$ layers, and the layer dependence of lateral interactions within the film.

For low-T growth with irreversible island formation, E_L^{ads} more than E_L^{Ag} will impact the kinetics of film growth and thus the film morphology. All results are presented for Ag adatom(s) at their preferred adsorption sites. For either isolated adatoms or a complete layer adsorbed directly on the

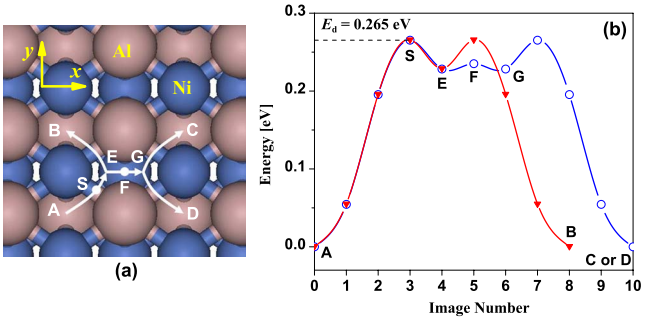

FIG. 3. (Color online) (a) Terrace diffusion paths from DFT +cNEB calculations for a Ag adatom on a NiAl(110) surface. (b) The corresponding cNEB energy curves.

NiAl(110) substrate, this is the Ni-(short) bridge site A, B, C, or D in Fig. 3(a).[10,11] For higher layers of the Ag(110) film, this is always the fourfold hollow site on the supporting Ag(110) layer.

Let $E_L^{\rm tot}$ denote the total energy per surface unit cell of a supported Ag(110) film of L layers together with the NiAl(110) substrate. $L=0$ corresponds to the clean substrate surface without any Ag layer. Then, it follows that $E_L=E_L^{\rm tot}-E_0^{\rm tot}$ is the total energy per unit cell associated with Ag atoms in the film and $E_L^{\rm Ag}=E_L/L$ for a 1×1 unit cell. The total energy per unit cell associated with atoms in layer L satisfies $\mu_L\equiv\Delta E_L=E_L-E_{L-1}$. A lower value of μ_L reflects a more stable film of thickness L. More specifically, a film of thickness L will be stable against bifurcation to films of thickness $L\pm1$ if the stability index $\Delta\mu_L=\mu_{L+1}-\mu_L$ is positive. $E_L^{\rm tot}$ and related quantities are calculated from a 1×1 supercell with a substrate of 11 NiAl(110) layers using a **k** mesh is $15\times21\times1$. All atoms are relaxed except those in the bottom 6 NiAl(110) layers. From Table II, μ_L, $\Delta\mu_L$, and $E_L^{\rm Ag}$ all exhibit bilayer oscillations reflecting enhanced stability for layers of even thickness, behavior attributed to QSE.[10,11,20,21]

Next, we consider the adsorption energy of an isolated Ag adatom on an $L-1$ layer film. Let $E_{L-1}^{\rm tot+1}$ denote the total energy of the film of thickness $L-1$ together with the adsorbed isolated adatom and $E_{\rm atom}=-0.335$ eV (from DFT) denote the energy of a completely isolated atom. We then have that

$$E_L^{\rm ads}=E_{L-1}^{\rm tot}+E_{\rm atom}-E_{L-1}^{\rm tot+1}. \quad (2)$$

Results shown in Table II are from calculations using a 3×4 supercell, a **k** mesh is $4\times4\times1$, and relaxing all atoms except the bottom NiAl(110) layer. Results vary little for more **k** points or a thicker NiAl(110) substrate. $E_L^{\rm ads}$ also exhibits bilayer oscillations due to QSE: stronger adsorption on films of odd thickness reflects enhanced stability of films with even thickness. Adsorption on top of a single-layer film is stronger than on the substrate by $\Delta E_{\rm ads}=0.047$ eV. Together with weaker adsorption on top of bilayer films, this promotes growth of bilayer islands and hinders population of the third layer.

The difference between energy per atom associated with a complete Lth layer and an isolated atom adsorbed in the same layer measures the total lateral attractive interaction energy per atom

$$E_L^{\rm int}=-[\mu_L-(-E_L^{\rm ads}+E_{\rm atom})]. \quad (3)$$

as reported in Table II (and defined to be positive). $E_L^{\rm int}$ is relevant for determining thin-film thermodynamics. To assess island nucleation behavior, instead one should consider the dominant nearest-neighbor (NN) attraction, E_b (defined to be positive) controlling the most stable isolated Ag dimers. Comparing the energies of an adsorbed dimer and of separated adsorbed constituent Ag atoms (with all Ag at preferred Ni-bridge sites), one obtains

$$E_b=2E_0^{\rm tot+1}-E_0^{\rm tot+2}-E_0^{\rm tot}, \quad (4)$$

where $E_0^{\rm tot+2}$ is the total energy of NiAl(110) substrate slab together with an adsorbed Ag dimer.

Allowing complete relaxation of the adatoms in the dimer, one obtains a "strong" bond strength of $E_{by}=0.074$ eV for adatoms on nearest-neighbor Ni bridge sites in the [001] direction (y direction), e.g., A and B in Fig. 3(a). Similarly, one obtains a "weak" bond strength of $E_{bx}=0.005$ eV for nearest-neighbor Ni bridge sites in the $[\bar{1}10]$ direction (x direction), e.g., A and D in Fig. 3(a). In these calculations, we used a 4×5 supercell, a **k**-point mesh of $6\times6\times1$, and relaxed substrate atoms except for the bottom layer of the 4-layer NiAl(110) substrate. Previous calculations comparing the energies for configurations of Ag addimers and separated

TABLE II. Magnitudes of various energies in electron volt (per surface unit cell) versus film thickness L in layers. Energies were determined from DFT calculations for Ag(110)/NiAl(110) or Ag/Ag(110)/NiAl(110) systems. A star denotes a value obtained by extrapolation to $L\to\infty$.

L	$E_L^{\rm Ag}$	$\mu_L=E_L-E_{L-1}$	$\Delta\mu_L$	$E_L^{\rm ads}$	$E_L^{\rm int}$
1	−2.838	−2.838	−0.0491	2.381	0.122
2	−2.863	−2.888	0.1339	2.428	0.124
3	−2.826	−2.754	−0.1312	2.324	0.095
4	−2.841	−2.885	0.1060	2.428	0.122
5	−2.829	−2.779	−0.0968	2.294	0.150
6	−2.836	−2.876	0.0821	2.412	0.129
7	−2.830	−2.793	−0.0658	2.265	0.194
∞	−2.828*	−2.832*	0	2.324*	0.173*

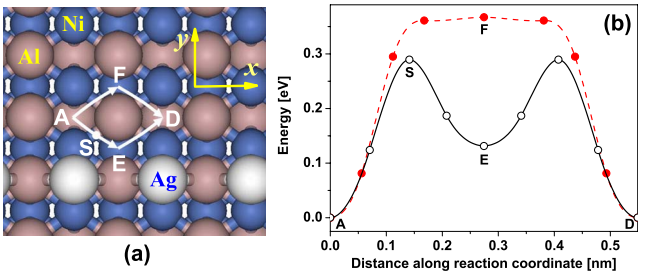

FIG. 4. (Color online) (a) Diffusion paths along a horizontal Ag island edge represented by a fixed horizontal Ag chain. (b) The DFT+cNEB energy curves correspond to two possible diffusion paths in (a).

Ag adatoms in a 3×4 supercell yielded $E_{by}=0.087$ eV and $E_{bx}=0.016$ eV.[11]

B. Diffusion barriers

The barriers for diffusion across terraces, E_d, along straight island edges, E_e, and around corners or kinks at island edges, E_{cr}, are key for controlling nucleation and lateral growth of islands. We obtain these barriers from a series of DFT+cNEB calculations. Figure 3 shows a diffusion path for a Ag adatom on NiAl(110) surface from the preferred Ni-bridge site, A, over a saddle point, S, to a shallow local minimum, E, at a threefold Ni-Al-Al site. It can then move directly to the nearest Ni-bridge site B in the y direction, or pass through the Al-bridge site F and the local minimum G in the x direction to Ni-bridge sites C or D.[11] Thus, the diffusion barrier is isotropic but the prefactor is ~2 times larger for the x direction versus y direction due to the rectangular unit cell. The DFT analysis shown in Fig. 3 yields $E_d=0.265$ eV using a supercell size of 2×3, a **k** mesh of $4\times4\times1$, and relaxing all atoms except the bottom layer of the 4-layer NiAl(110) slab.

Diffusion along straight island edges is assessed from the energy landscape for a Ag atom moving along a fixed chain of Ag atoms. We assess diffusion around corners from consideration of a Ag atom moving around a single fixed Ag atom. Convergence tests of DFT+cNEB calculations show that a small 3×4 supercell is sufficient. Our calculations use a **k** mesh that is $4\times4\times1$ and substrate atoms are relaxed except the bottommost layer of the 4-layer NiAl(110) substrate is fixed. We find that diffusion along horizontal edges is somewhat inhibited, so the barrier is a relevant model parameter. Diffusion along vertical edges which is facile (so model behavior is insensitive to the precise value of the barrier), and direct diffusion around corners is essentially inoperative (so the barrier is not relevant).

Figure 4(a) shows two possible diffusion paths along a horizontal island edge. Figure 4(b) shows DFT energies along path A-E-D path revealing a saddle point at site S which determines the energy barrier of 0.289 eV. Figure 4(b) also shows flatter energy along the A-F-D path with an energy barrier of 0.367 eV at F approximately equal to the sum $E_d+E_{by}=0.265+0.087=0.352$ eV. Thus, the diffusion path A-E-D dominates and the effective edge-diffusion barrier, $E_{ex}=0.289$ eV, is comparable to E_d.

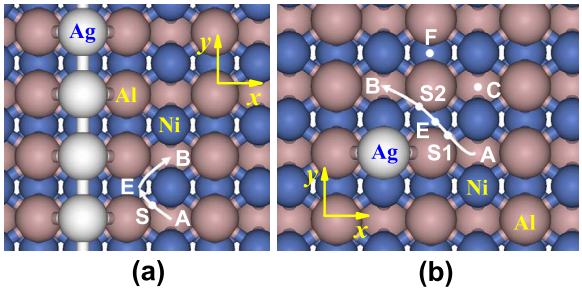

FIG. 5. (Color online) (a) Diffusion path along a vertical Ag island edge represented by a fixed vertical Ag chain. (b) Diffusion path around an island corner represented by a single fixed Ag adatom.

Figure 5(a) shows the preferred diffusion path A-E-B along a vertical step edge. Edge diffusion is facile as the energy at the saddle point, S, is only about $E_{ey}\sim0.13$ eV above that for site A. This is not surprising since the diffusing Ag adatom at this transition state is strongly attracted to other Ag adatoms in the vertical chain representing the island edge. DFT indicates an energy for site E somewhat below that for A, an issue discussed further in Sec. VII.

For corner rounding, Fig. 5(b) indicates one saddle point S1 with energy 0.20 (0.27) eV above that at A (B), and another S2 with energy 0.36 (0.43) eV above A (B). Between S1 and S2 is a local minimum, E, with energy 0.12 (0.19) eV above A (B). Thus, a Ag adatom attempting to round the corner from A can readily hop to E but will tend not to continue directly to B. Instead, it would more easily hop to C then F then B. So the direct pathway is not operative and corner rounding tends to occur via detachment and reattachment.

V. ATOMISTIC LATTICE-GAS MODEL AND KMC SIMULATION

A realistic and comprehensive atomistic model for Ag island formation on NiAl(110) must include not only random deposition of Ag, subsequent terrace diffusion and aggregation of Ag adatoms into islands, and diffusion along the edges of thus formed islands, but also detachment from island edges and interlayer transport. It is necessary to specify intralayer and interlayer hop rates for a large number of configurations with adatoms at or near island edges. Specification of all these barriers must be consistent with detailed balance and will thus reflect Ag adatom adsorption and interaction energies. Our general prescription for these barriers is crafted to incorporate precise DFT values for terrace and straight edge-diffusion processes. Below, $E_b^{\rm init}=E_{bj}^{\rm init}>0$ will denote the total lateral interaction energy before hopping for either a first-layer ($j=1$) or second-layer ($j=2$) Ag adatom.

For *intralayer hopping*, "pure" edge hops where the Ag adatom has an NN edge atom both before and after hopping are described by a barrier $E_{\rm edge}=E_{ey(x)}+(E_b^{\rm init}-E_{bx(y)})$ for hopping in the $y(x)$ direction. Thus, one has $E_{\rm edge}=E_{ey(x)}$ for diffusion along straight edges. For all other intralayer hops, including terrace diffusion and attachment-detachment from island edges, one sets $E_{\rm act}=E_d+E_b^{\rm init}$, so that the barrier for all

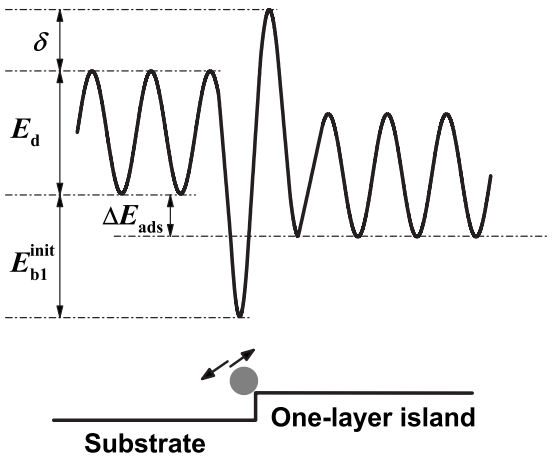

FIG. 6. Schematic of the PES for an adatom traversing the step edge of a single-layer island.

attachment processes is $E_{\text{attach}}=E_d$. Detachment from y edges is facile with a barrier of $E_{\text{act}}=E_d+E_{bx}$ only slightly above E_d due to weak interactions E_{bx}. The same low barrier applies for corner rounding from y edge to x edge. Detachment from kinks to terraces is operative, its barrier of $E_{\text{kink}}=E_d+E_{by}+E_{bx}$ only slightly exceeding that for dissociation of the most stable dimers aligned in the y direction of $E_{\text{diss}}=E_d+E_{by}$.

For *interlayer hopping*, QSE becomes relevant. For upward hopping to the top of first-layer islands from their edges, i.e., for step climbing, we assign a barrier of

$$E_{\text{up}} = E_d + E_{b1}^{\text{init}} + \delta, \tag{5}$$

where δ accounts for a possible additional step climbing barrier and here E_{b1}^{init} corresponds to first-layer adatom interactions (nonzero for upward hopping). δ will correspond to the standard definition of an Ehrlich-Schwoebel barrier in the absence of QSE. Thus, one has facile upward transport at straight y edges with barrier $E_{\text{up}} \approx E_d+E_{bx}+\delta$ barely exceeding E_d (assuming small δ) due to weak interactions E_{bx}. For downward hopping, detailed-balance considerations impose a barrier of

$$E_{\text{down}} = E_d + E_{b2}^{\text{init}} + \delta + \Delta E_{\text{ads}}, \tag{6}$$

where E_d is again the diffusion barrier for Ag on NiAl(110) (not for Ag on top of single-layer islands) and E_{b2}^{init} corresponds to second-layer adatom interactions. The excess adsorption energy for Ag in the second layer relative to the first layer, $\Delta E_{\text{ads}}=0.047$ eV>0, increases the barrier for downward hopping thus facilitating bilayer island growth. Figure 6 illustrates the PES for an adatom traversing a step at the edge of a monolayer island (where $E_{bj}^{\text{init}}=0$ for an isolated adatom).

KMC simulations were performed for our atomistic lattice-gas model of film growth on a substrate represented by a rectangular lattice of adsorption sites. The model includes all the above hopping processes with barriers as specified and a common prefactor of 10^{13}/s. Deposition at the experimental rate is operative until the target coverage of adsorbed Ag is reached after which only hopping processes are active. For simplicity, we treat second-layer sites as directly above first-layer sites rather then in their true fcc locations. This will not significantly impact shapes of larger islands or the degree of bilayer formation but may have some slight effect for small islands formed at low T. Diffusion processes in the second layer are treated by the same formulation used for the first layer. Our DFT analysis suggests that the strong bond E_{by} is higher than in the first layer, so we have performed simulations with values equal to and above that for the first layer (and use 0.18 eV unless otherwise stated). Other second-layer parameters are equated to first-layer values. Table II shows adsorption in the third layer is 0.10 eV weaker than in the second layer. Thus, formation of the third layer is strongly inhibited (and precluded in our modeling).

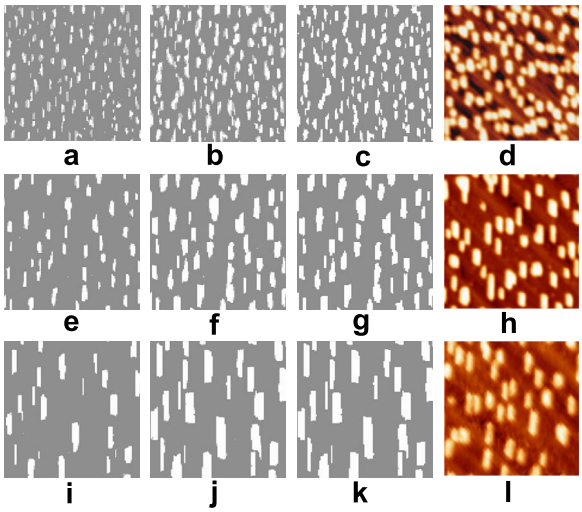

FIG. 7. (Color online) Images (46×46 nm^2) of Ag islands on NiAl(110) for $F=0.0066$ ML/s. From left to right: KMC simulation with $E_{by}=0.086$ eV, $E_{bx}=0.036$ eV, and $\delta=0$ after deposition of 0.1 BL, 0.2 BL, and ~10 min later; STM image ~10 min after deposition of 0.2 BL ($I=0.5$ nA, $V=+1.0$ V). Light gray (white) denotes first (second) layer of Ag. [(a)–(d)] $T=127$ K; [(e)–(h)] $T=140$ K; and [(i)–(l)] $T=150$ K.

VI. KMC SIMULATION RESULTS

A. Island formation during deposition

Figure 7 shows results for KMC simulation of film growth at 127, 140, and 150 K, depositing 0.2 BL of Ag using values of parameters indicated above except for increasing E_{bx} to 0.036 eV, and setting $\delta=0$. (With a smaller E_{bx}, islands are too elongated.) Results reveal near-complete bilayer island formation even during deposition. Experimental STM images are also shown to demonstrate the success of the model in predicting trends in island density and shape with varying T. STM images are acquired roughly 10 min after completion of deposition. Thus, simulations are also continued into this postdeposition regime where there is a driving force for islands with only partial occupation of the second layer to evolve towards complete bilayer islands.

We have performed a substantial set of simulations varying key energetic parameters to assess their influence on the

TABLE III. KMC simulation results assessing the extent of second-layer formation as a function of key energetic parameters (in millielectron volt) at 140 K with $F=0.0066$ ML/s. N_2 is the number of second-layer atoms and N_1 is the number of exposed first-layer atoms, so that the total number of adatoms is $N_1+2N_2=1475$ when deposition is completed. We show the ratio $R=N_2/N_1$ both at the end of deposition (at ~45 s) and later (at ~595 s). Subscripts 1 and 2 of E_{bx} or E_{by} denote Ag interactions for adsorption on top of the NiAl(110) substrate surface and in the first Ag(110) layer, respectively.

E_{by1}	E_{bx1}	E_{by2}	E_{bx2}	ΔE_{ads}	δ	R(~45 s)	R(~595 s)
86	36	140	36	47	0	687/101	737/1
86	36	180	36	47	0	689/97	737/1
110	36	180	36	47	0	609/257	735/5
126	36	180	36	47	0	358/759	607/261
110	50	180	50	47	0	464/547	706/63
120	50	180	50	47	0	343/789	527/421
86	86	180	36	47	0	266/943	401/673
86	86	86	86	47	0	253/969	463/603
86	36	187	36	0	0	18/1439	668/139
86	36	180	36	47	20	564/347	736/3
86	36	180	36	47	40	307/861	714/47
86	36	180	36	47	50	212/1051	619/237
86	36	180	36	47	60	201/1073	449/577

propensity for bilayer growth, see Table III. Three general trends are investigated: (i) varying lateral bonding while retaining $\Delta E_{\text{ads}}>0$ and setting the step climbing barrier $\delta=0$; (ii) setting $\Delta E_{\text{ads}}=0$; and (iii) increasing $\delta>0$. For (i), just slightly increasing the strong bond to $E_{by}=0.11$ eV results in partial bilayer islands at the end of deposition, but restructuring to almost complete bilayer islands still occurs in the next 10 min. Further increases in first-layer bonding inhibit even postdeposition formation of bilayer islands. For (ii), bilayer island formation does not occur even with stronger second-layer bonding, so $\Delta E_{\text{ads}}>0$ is key. For (iii), only partial bilayer islands occur at the end of deposition for $\delta \geq 0.02$ eV, but complete bilayer islands still form within 10 min if $\delta \leq 0.04$ eV.

We attribute *facile bilayer island formation* to the presence of *anisotropic interactions* and specifically to weak interactions in the $[\bar{1}10]$ direction. Diffusing atoms can easily ascend straight island edges aligned in the [001] direction. Also, atoms can escape first-layer kinks by breaking a single strong bond thereby enabling upward transport. To support these ideas, simulations for our model have been performed after first increasing E_{bx1} to equal E_{by1} (cf. Table III) to produce isotropic first-layer interactions. Results shown in Fig. 8 reveal negligible bilayer island formation since kink adatoms are trapped in the first layer by two strong bonds. Of course, now shapes of the first-layer islands are isotropic. The nonzero second-layer population is presumably due primarily to direct deposition into this layer.

One expects that island formation in this system at the lowest $T\sim 130$ K will be at least close to irreversible ($i=1$). This might seem inconsistent with bilayer island formation. Irreversibility implies that the rate of dissociation of the most stable dimers is below the rate of aggregation (i.e., the rate at which diffusing atoms aggregate with dimers and other islands). Then, dimers convert to larger more stable islands before dissociation. For isotropic systems, typically growth does lead to more stable islands where essentially all atoms, including those at kink sites, are "locked in" by multiple strong bonds. However, in this anisotropic system, adatoms at kink sites have only a single strong bond and thus can escape on the time scale of deposition (which is much longer than the time scale of aggregation) to climb to the second layer as noted above.

Finally, we discuss further island growth shapes. Recall that bilayer Ag islands on NiAl(110) become increasingly elongated up to 300 K, whereas monolayer Ag islands on Ag(110) become broader above about 220 K. The bilayer structure of Ag/NiAl(110) islands appears to "lock in" the growth structure and inhibits shape equilibration. To test this hypothesis, we have performed simulations using our model retaining the diffusion barriers and lateral interaction values for Ag/NiAl(110), but inhibiting bilayer island formation. The results shown in Fig. 9 reveal that now island shapes do become broader even at quite low T analogous to Ag/Ag(110) homoepitaxy. Simulation movies reveal that the monolayer islands at higher T are quite dynamic in contrast to the nearly "frozen" bilayer islands.

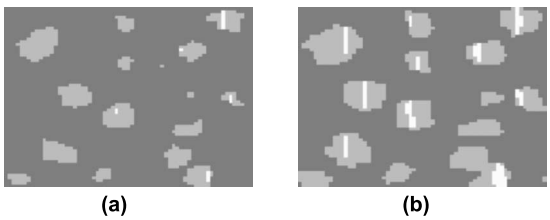

FIG. 8. KMC simulated images (27×19 nm^2) of island formation with isotropic interactions at $T=140$ K. All parameters are the same as those of Fig. 7 except E_{bx} is set equal to $E_{by}=0.086$ eV. Light gray (white) denotes first (second) layer of Ag. (a) 0.1 BL and (b) 0.2 BL.

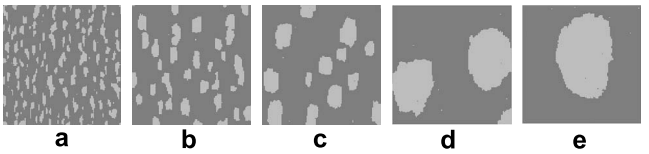

FIG. 9. KMC images (46×46 nm^2) of single-layer island formation with anisotropic interactions. All parameters are the same as those of Fig. 7 except δ is set to infinity to inhibit hopping up of first-layer adatoms. Also, adatoms directly deposited on top of the first Ag(110) layer are neglected. (a) $T=127$ K and $\theta=0.2$ ML; (b) $T=140$ K and $\theta=0.2$ ML; (c) $T=150$ K and $\theta=0.2$ ML; (d) $T=175$ K and $\theta=0.2$ ML; and (e) $T=190$ K and $\theta=0.13$ ML.

B. Postdeposition coarsening

Our simulation model has also been applied to study postdeposition coarsening of island distributions (retaining the same energetic parameters as for deposition studies). Our coarsening simulations incorporate exactly the same protocol for ramping up the temperature (following deposition at 130 K) as used in experiment. See Fig. 10(a). Uncertainties in experimental temperatures (shown) are ±2.5 K. We find that deposition at 130 K and high $F=0.056$ ML/s produces islands with primarily monolayer structure. However, in about the first 10 min after deposition, these islands either dissolve or convert to primarily bilayer structure even with T held at 130 K. When T is subsequently increased, there is significant coarsening. The decrease in simulated island density matches well the experimental observations.

We have already provided some discussion of uncertainties in experimental island densities in Sec. IV. One factor is the finite number, M, of islands counted (i.e., the finite sample size) for each data point. However, for our coarsening data, typically on the order of $M\sim1000$ islands are counted at 130 K, and a few hundred for higher T, so corresponding uncertainties are small. A more significant factor is the difficulty in determining from STM images whether nearby islands are connected (and thus should be counted as a single island to be consistent with the percolation-like algorithm used in the simulations). The associated uncertainty is substantial in this coarsening study since the density of islands remains high and their size small (compared with deposition studies in Table I) at least up to 60 min or 170 K. Based on detailed examination of the STM images, we as-

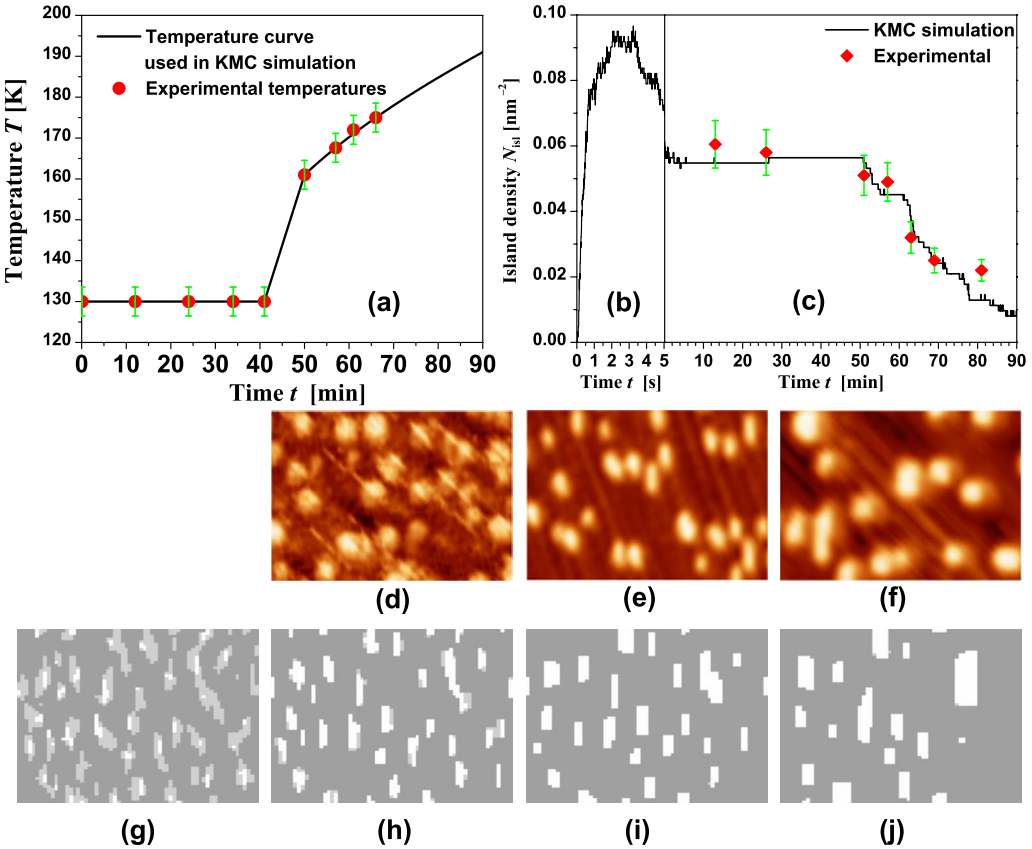

FIG. 10. (Color online) (a) Experimental temperature points as a function of time t after the deposition ($I=0.5$ nA, $V=+1.0$ V, and $F=0.056$ ML/s) of 0.14 BL Ag on NiAl(110) at $T=130$ K, and the corresponding fitting curve, which is used in the following temperature-dependent KMC simulation. (b) KMC simulation of island density versus time during deposition. (c) A comparison between the simulated and experimental island density as a function of time and temperature. Uncertainties in simulated values are $\pm12\%$ at 130 K, increasing to $\pm18\%$ at 175 K. Uncertainties in experimental values are shown. See the text for discussion. (d), (e), and (f) are the STM images at $t=12$ min, 57 min, and 66 min corresponding to $T=130$ K, 168 K, and 175 K, respectively. (g) The KMC image just after the deposition. Light gray (white) denotes first (second) layer of Ag. (h), (i), and (j) are the KMC images corresponding to (d), (e), and (f), respectively. The KMC energetic parameters are the same as those of Fig. 7. The size of any image is 27×19 nm^2.

sign uncertainties to the data in Fig. 10 of ±15%.

For the simulations, uncertainty comes only from sample size, and we estimate of the percentage uncertainty in the island density from $100(C/M)^{1/2}$ using $C=0.5$. Since these simulations for long times were very expensive, a small system size was used producing a larger uncertainty in the simulated island density of ±12% at 130 K (where $M\sim 40$), increasing to ±18% at 175 K. Finally, we remark that the simulated $N_{\rm isl}\sim 60\times 10^{-3}$ nm^{-2} for deposition at 130 K with $F=0.056$ ML/s is consistent with the lower $N_{\rm isl}\sim 35\times 10^{-3}$ nm^{-2} for a similar $T=127$ K in Table I where F is lower by an order of magnitude.

There exist extensive analyses of equilibrium island shapes and of coarsening for monolayer metal islands.[28,29] The equilibrium shape corresponds to minimizing the step (free) energy for fixed island size and the driving force for coarsening is a reduction in the overall step energy for a distribution of islands. Coarsening pathways include Ostwald ripening (OR: net detachment of atoms from smaller islands and reattachment to larger ones) and Smoluchowski ripening (SR: cluster diffusion and coalescence). Our simulations for bilayer Ag islands on NiAl(110) indicate a predominance of Ostwald ripening but experimental determination of the dominant pathway requires more detailed studies which we plan to perform.

For monolayer islands, one typically estimates the step energy as half the strength of the broken bonds per unit length of the step edge (noting that broken bonds are shared). Thus, for monolayer rectangular fcc(110) islands, their equilibrium aspect ratio equals the ratio of step energies for the two edges, which is accurately approximated by the ratio of the nearest-neighbor interaction strengths for the two directions. For rectangular bilayer fcc(110) islands in the presence of QSE, the situation is more complicated. For simplicity, assume that these islands have a perfect (complete) bilayer structure. Then, it is important to note that as an island of fixed size changes shape, i.e., as it changes aspect ratio, the number of atoms in the second layer changes. The same is true if two smaller islands are combined to form a larger island with the same total number of atoms. Thus, the change in total energy of the system is impacted by the difference, $\Delta E_{\rm ads}$, in adsorption energy for the substrate and on top of the first layer. If one defines an effective step energy for these bilayer islands which would describe the driving force for coarsening, then this would involve $\Delta E_{\rm ads}$ as well as the strengths of bonds broken at island edges in both the first and second layer.[50]

Next, we briefly discuss coarsening kinetics for OR. The effective barrier for coarsening via OR is usually written as $E_{\rm eff}=E_d+E_{\rm form}+\delta_{\rm att}$. Here, E_d is the terrace diffusion barrier, $E_{\rm form}$ is the energy cost to detach an island atom (from a suitable kink site), and $\delta_{\rm att}$ represents any effective attachment barrier. Although not tested, this result should apply for OR in anisotropic fcc(110) homoepitaxial systems,[51] with the caveat that unusual behavior can occur at low T.[52,53] For bilayer Ag islands on NiAl(110), $E_d=0.265$ eV is the diffusion barrier for Ag on NiAl(110). Detachment from a second-layer kink site will cost an energy $E_{\rm form}=E_{by2}+E_{bx2}+\Delta E_{\rm ads}$. If there exists a substantial step climbing barrier, then one has a nonzero $\delta_{\rm att}\approx\delta$. A more detailed discussion will be presented elsewhere.

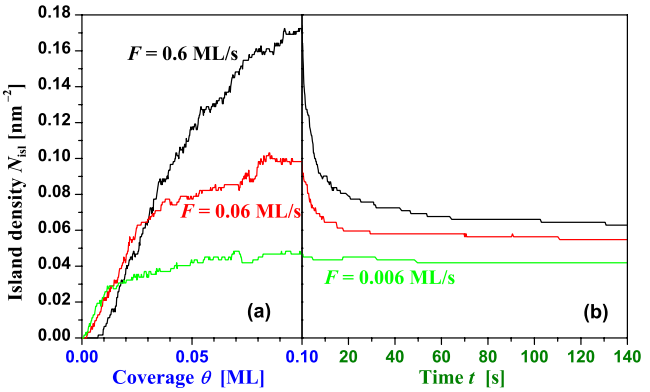

FIG. 11. (Color online) KMC simulated island density $N_{\rm isl}$ as a function of coverage θ or time t during deposition at $T=130$ K for three different fluxes and subsequent to deposition also at $T=130$ K. Energetic parameters are the same as those of Fig. 7. (a) $N_{\rm isl}$ versus θ during the deposition. The total Ag coverage is 0.1 ML. (b) $N_{\rm isl}$ versus t after the deposition.

Finally, we consider the possibility of an unusual dependence of coarsening kinetics on flux. This is motivated by observations for quantum islands of Pb on Si(111): deposition with higher F naturally produce a higher initial island density but surprisingly a lower postcoarsening island density.[54] The reason is that in this system, high-F deposition produces a larger population of islands with unstable heights which are susceptible to rapid coarsening.[30] For the Ag/NiAl(110) system, deposition with higher F can produce a higher population of monolayer or incomplete bilayer islands which might also be amenable to rapid coarsening. Simulation results shown in Fig. 11 do reveal more rapid coarsening for higher F but postcoarsening island densities are still higher.

VII. DISCUSSION AND SUMMARY

Detailed atomistic modeling has been presented that successfully describes and elucidates the kinetics of facile Ag bilayer island formation on NiAl(110) at low T. In addition, the same model is effective in describing postdeposition coarsening. This success reflects the feature that the model accurately captures both thermodynamic and kinetic aspects of this system, the choice of energetic parameters being guided by extensive DFT analysis.

Our modeling does likely oversimplify the description of some finer details of the structure and kinetics in this Ag/NiAl(110) system. Recall that our DFT analysis in Sec. IV indicated a slightly lower energy of a diffusing atom near an Al-bridge site close to a vertical island edge [E in Fig. 5(a)] rather than at the standard Ni-bridge site. Similarly, we find that for an adjacent vertical pair of Ag atoms at this step edge, Al-bridge site configuration close to the island edge is slightly preferred over the standard Ni-bridge sites. These motifs reflect the "hex" structure described in Appendix A.

Thus, it is plausible that in the initial stages of Ag adatom aggregation to form islands, monolayer structures with hex-type motifs do appear. However, except perhaps for very low T, one expects that such island structures if formed must

readily convert to bilayer fcc(110) structures as they grow larger, their adatoms returning to standard adsorption sites. In this case, the current model would not precisely describe the initial stages of island formation, but would effectively describe subsequent lateral growth and bilayer development. A more precise description would require off-lattice or multisite lattice-gas modeling. Given this more complex picture, one might anticipate that that deposition at very low T and higher flux could trap islands in the local hex structure at least initially. Our STM data for deposition at 130 K with high $F=0.056$ ML/s up to ~15 min after deposition provides some indication that this is the case (although image quality is insufficient for definitive determination of structure).

While many other systems exhibit bilayer or multilayer quantum islands, a detail atomistic-level characterization of the kinetics has been lacking. For Ag/NiAl(110), the strong anisotropy in bonding is a key factor responsible for the observed facile bilayer island formation. The feature that strong anisotropy facilitates growth and relaxation kinetics for bilayer and multilayer islands should apply to other heteroepitaxial systems.

ACKNOWLEDGMENTS

The modeling component of this work by Y.H. and J.W.E. was supported by NSF under Grant No. CHE-0809472, as were experimental contributions of F.Q. and P.A.T. Computational support at NERSC was provided by the U.S. DOE. Experimental contributions of B.U., D.J., and C.J.J. were supported by U.S. DOE BES-Materials Sciences. DFT analysis by D.J.L. was supported by U.S. DOE BES-Chemical Sciences. The work was performed at Ames Laboratory which is operated for the U.S. DOE by ISU under Contract No. DE-AC02-07CH11358.

APPENDIX A: STRUCTURE OF Ag OVERLAYERS ON NiAl(110)

Figures 12(a)–12(c) show monolayer versions of various low-energy Ag film structures on NiAl(110) as determined by DFT analysis. Figure 12(a) shows a monolayer Ag(110) structure. We claim that observed Ag islands correspond to the bilayer version of this structure (which is more stable than the monolayer version) with second-layer atoms at the fourfold hollow sites. See also Ref. 10. The height of monolayer (bilayer) fcc(110) structures is 0.21 nm (0.34 nm), the latter matching experimental bilayer island height. Figure 12(b) shows a monolayer "double-chain" structure where rows of atoms in the (110) structure have paired. The height of this monolayer structure is 0.22 nm, too low to match experiment. The bilayer version of this structure with second-layer double chains between first-layer chains is not very stable. Figure 12(c) shows a monolayer "square-hex" structure with height of 0.23 nm, too low to match experiment. The bilayer version of this structure has the second-layer hex motifs sitting above monolayer square motifs and visa versa. It is quite stable but has a height of 0.49 nm, too high to match experiment.

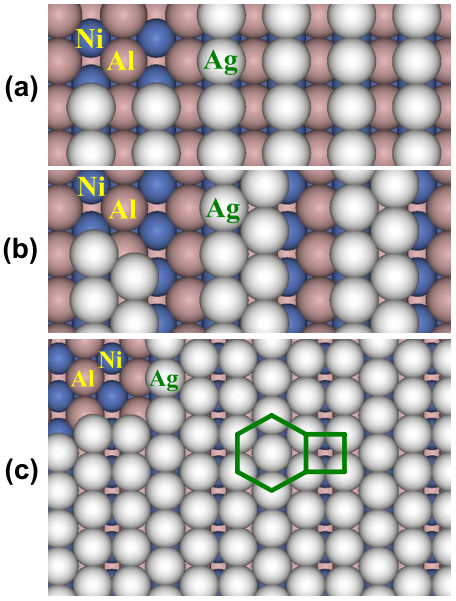

FIG. 12. (Color online) (a) Ag(110) monolayer, (b) Ag double-chain monolayer, and (c) Ag square-hex monolayer structures on NiAl(110).

APPENDIX B: DFT ANALYSIS OF Ni SUBSTITUTIONAL DEFECT ON NiAl(110)

A Ni-substitutional defect on NiAl(110), where an Al atom in the surface layer is replaced by Ni, is shown in Fig. 13. Below, we calculate modified adsorption energies for a Ag adatom and addimer in the vicinity of this defect. In these DFT calculations, we use a 4×5 supercell, a **k**-point mesh of $6\times6\times1$, and relax all atoms except the bottommost layer of the 4-layer NiAl(110) substrate.

For a Ag adatom, the preferred adsorption site is at D shown in Fig. 13 (shifted ~0.017 nm toward the Ni defect from the Ni-bridge site). The corresponding adsorption energy $E_{\mathrm{def}}^{\mathrm{ads}}=2.484$ eV, which is larger by $\Delta E_{\mathrm{def}}=0.103$ eV than $E^{\mathrm{ads}}=2.381$ eV (see Table II, and also note that subscript "$L=1$" has been omitted here) for the preferred adsorption site, e.g., site A in Fig. 3(a), on a defect-free surface. Similar to the adsorption energy for an adatom, we define the total adsorption energy for an addimer, E^{adsd}, by correspondingly replacing "adatom" with "addimer" in Eq. (2). For a defect-free NiAl(110) surface, the most stable Ag addimer sits on sites A and B in Fig. 3(a) with $E^{\mathrm{adsd}}=4.839$ eV. For a Ni defect, the preferred adsorption sites are E and F shown in

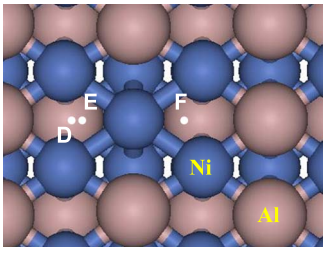

FIG. 13. (Color online) A defect on NiAl(110) surface formed by replacing a surface Al atom with a Ni atom.

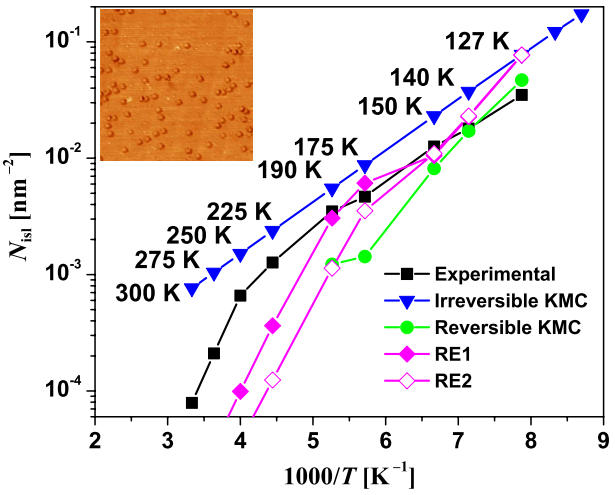

FIG. 14. (Color online) Island density $N_{\rm isl}$ versus temperature T. Comparison of KMC simulation results for irreversible ($i=1$) and reversible homogeneous island formation (the latter from the model of Sec. V), the mean-field rate equation model (RE1 and RE2, see text) for defect-enhanced nucleation with parameters described in the text, and experimental data. The inset (upper left) shows an STM image (100×100 nm^2) of surface point defects observed after one standard sample preparation procedure. Features appear similar to point defects observed by STM on $Au_3Cu(001)$ (Ref. 45) and by another group on NiAl(110) (Ref. 43).

Fig. 13. The corresponding $E_{\rm def}^{\rm adsd}=5.050$ eV, which is 0.211 eV larger. The preferred adsorption sites E and F correspond to an addimer bond length reduced by ~25% relative to its standard value. Thus, the effective bond strength for the dimer at the defect is $E_{bd}=E_b+0.211$ eV$-\Delta E_{\rm def}=0.195$ eV.

APPENDIX C: RATE EQUATION ANALYSIS OF DEFECT-ENHANCED NUCLEATION

The decrease in experimental island density, $N_{\rm isl}$, with increasing higher T is slower than predicted by our model for homogeneous nucleation. This may due to the neglect of heterogeneous nucleation at defects such as the Ni-substitutional point defect. An STM image of point defects obtained after one standard NiAl(110) sample preparation procedure is shown as an inset in Fig. 14. As noted in Sec. III, this observation of defects is consistent with those of other groups. Our proposal for competitive homogeneous and heterogeneous nucleation is assessed by developing a mean-field rate equation (RE) model. The goal is to identify viable ranges for the defect density and adatom bonding which lead to enhanced nucleation.

The key ingredients of the model are as follows: (i) reversible homogeneous nucleation of Ag islands on terraces controlled by terrace diffusion with barrier $E_d=0.265$ eV and a strong adatom bond of $E_b=0.087$ eV. For simplicity, we assign a critical size of $i=3$ (i.e., islands of size more than 3 atoms are stable). We assign capture numbers for substable islands as $\sigma_{s<4}=1$ and for all stable islands as $\sigma_x=5$ (a choice based on simulation analyses). Rates for detachment from islands are governed by detailed balance and thus involve E_b. Since mean-field modeling artificially enhances dimer dissociation rates,[38] we further reduce detachment rates by a factor of $c=0.5$ to mimic exact behavior. (ii) Reversible heterogeneous nucleation of Ag islands at defects is partly due to enhanced binding of adatoms at defects by an amount $\Delta E_{\rm def}$. Adatoms can thus reversibly attach and detach from defect sites, where the detachment rate is influenced by $\Delta E_{\rm def}$ according to detailed balance. In addition, we allow for stronger adatom bonding at defects with strength $E_{bd}>E_b$. Capture numbers, the critical size, and the factor c are chosen as for homogeneous nucleation, and we choose the capture number for empty defects as $\sigma_0=1$.

It is convenient to introduce the following notation. First, let N_s and M_s denote the density of islands of size s on terraces and at defects, respectively, and let $N_x=N_4+N_5+\cdots$ and $M_x=M_4+M_5+\cdots$ denote the corresponding densities of stable islands. Thus, if M denotes the density of defects, then $M_0=M-M_1-M_2-M_3-M_x>0$ denotes the density of defects free of Ag atoms of islands. Second, let $h\equiv\nu e^{-\beta E_d}$ denote the terrace hop rate. Then, we introduce rates $K_s=\sigma_s h N_1 N_s$ and $K_s^d=\sigma_s h N_1 M_s$ for aggregation of diffusing adatoms with terrace and defect islands of size $s<4$, respectively, and $F_s=c\sigma_s h e^{-\beta E_b}N_s$ and $F_s^d=c\sigma_s h e^{-\beta E_{bd}}M_s$ for detachment of adatoms from terrace and defect islands of size s, respectively. For rates of aggregation with stable islands, the subscript s is replaced by x. Then, one obtains the equations

$$\frac{dN_1}{dt}=F\left(1-\frac{\theta}{2}\right)-2K_1-K_2-K_3-K_x-K_0^d-K_1^d-K_2^d-K_3^d-K_x^d+2F_2+F_3+F_2^d+F_3^d+\sigma_0 h e^{-\beta\Delta E_{\rm def}}M_1, \quad \text{(C1)}$$

$$\frac{dM_1}{dt}=K_0^d-K_1^d+F_2^d-\sigma_0 h e^{-\beta\Delta E_{\rm def}}M_1, \quad \text{(C2)}$$

$$\frac{dN_2}{dt}=K_1-K_2-F_2+F_3, \quad \text{(C3)}$$

$$\frac{dM_2}{dt}=K_1^d-K_2^d-F_2^d+F_3^d, \quad \text{(C4)}$$

$$\frac{dN_3}{dt}=K_2-K_3-F_3, \quad \frac{dM_3}{dt}=K_2^d-K_2^d-F_3^d, \quad \text{(C5)}$$

$$\frac{dN_x}{dt}=K_3, \quad \frac{dM_x}{dt}=K_3^d. \quad \text{(C6)}$$

To recover experimental behavior for T up to 190 K, we can choose $\Delta E_{\rm def}=0.103$ eV and $E_{bd}=0.195$ eV, from DFT values, and a defect density of $M=0.001$/site $=0.0085$ nm^{-2} (chosen below the typical island density for lower T). With this parameter choice, $N_{\rm isl}$ still decreases more quickly than in experiment above 190 K (shown as RE1 in Fig. 14). If one reduces the value of E_{bd} for trimers at defects to equal E_b, then the decrease in $N_{\rm isl}$ is more dramatic (RE2 in Fig. 14). On the other hand, inhibition of the rapid decrease in $N_{\rm isl}$ just above 190 K can be achieved by increas-

ing E_{bd}. However, the discrepancy between the model and experiment is likely real, perhaps reflecting the neglect of heterogeneous nucleation at other types of defects.

We offer one final comment on low-T behavior, specifically regarding comparison of predictions of the full model, behavior for $i=1$, and RE predictions. Reversibility around 140 K would tend to give steeper Arrhenius slope than $E=E_d/3$ for an $i=1$ model. However, there is also some post-deposition coarsening of the small islands formed in experiment at low T which lowers the measured density thus the Arrhenius slope at low T. Due to these competing effects, the slope appears to match that for $i=1$ behavior.

*octavian2009@gmail.com

†Present address: Department of Chemical Engineering, Massachusetts Institute of Technology, Cambridge, Massachusetts 02139.

[1] E. Bauer, Z. Kristallogr. **110**, 372 (1958).
[2] P. J. Schmitz, W.-Y. Leung, G. W. Graham, and P. A. Thiel, Phys. Rev. B **40**, 11477 (1989).
[3] S.-L. Chang, J.-M. Wen, P. A. Thiel, S. Günther, J. A. Meyer, and R. J. Behm, Phys. Rev. B **53**, 13747 (1996).
[4] R. Pentcheva and M. Scheffler, Phys. Rev. B **61**, 2211 (2000).
[5] B. Voigtländer, G. Meyer, and N. M. Amer, Phys. Rev. B **44**, 10354 (1991).
[6] C. Tölkes, P. Zeppenfeld, M. A. Krzyzowski, R. David, and G. Comsa, Phys. Rev. B **55**, 13932 (1997).
[7] H. W. Chang, F. T. Yuan, Y. D. Yao, W. Y. Cheng, W. B. Su, C. S. Chang, C. W. Lee, and W. C. Cheng, J. Appl. Phys. **100**, 084304 (2006).
[8] H. Hoster, T. Iwasita, H. Baumgärtner, and W. Vielstich, Phys. Chem. Chem. Phys. **3**, 337 (2001).
[9] A. Verdini, L. Floreano, F. Bruno, D. Cvetko, A. Morgante, F. Bisio, S. Terreni, and M. Canepa, Phys. Rev. B **65**, 233403 (2002).
[10] B. Unal, F. Qin, Y. Han, D.-J. Liu, D. Jing, A. R. Layson, C. J. Jenks, J. W. Evans, and P. A. Thiel, Phys. Rev. B **76**, 195410 (2007).
[11] Y. Han, B. Unal, F. Qin, D. Jing, C. J. Jenks, D.-J. Liu, P. A. Thiel, and J. W. Evans, Phys. Rev. Lett. **100**, 116105 (2008).
[12] A. R. Smith, K.-J. Chao, Q. Niu, and C.-K. Shih, Science **273**, 226 (1996).
[13] D.-A. Luh, T. Miller, J. J. Paggel, M. Y. Chou, and T.-C. Chiang, Science **292**, 1131 (2001).
[14] K. L. Man, Z. Q. Qiu, and M. S. Altman, Phys. Rev. Lett. **93**, 236104 (2004).
[15] B. J. Hinch, C. Koziol, J. P. Toennies, and G. Zhang, Europhys. Lett. **10**, 341 (1989).
[16] R. Otero, A. L. Vázquez de Parga, and R. Miranda, Phys. Rev. B **66**, 115401 (2002).
[17] V. Fournée, H. R. Sharma, M. Shimoda, A. P. Tsai, B. Unal, A. R. Ross, T. A. Lograsso, and P. A. Thiel, Phys. Rev. Lett. **95**, 155504 (2005).
[18] B. Ünal, V. Fournée, P. A. Thiel, and J. W. Evans, Phys. Rev. Lett. **102**, 196103 (2009).
[19] F. K. Schulte, Surf. Sci. **55**, 427 (1976).
[20] Y. Han, J. W. Evans, and D.-J. Liu, Surf. Sci. **602**, 2532 (2008).
[21] Y. Han and D.-J. Liu, Phys. Rev. B **80**, 155404 (2009).
[22] R. A. Miron and K. A. Fichthorn, Phys. Rev. B **72**, 035415 (2005).
[23] Z. Kuntová, M. C. Tringides, and Z. Chvoj, Phys. Rev. B **78**, 155431 (2008).
[24] Y. Han, F. Liu, S.-C. Li, J.-F. Jia, Q.-K. Xue, and B.-J. Lee, Appl. Phys. Lett. **92**, 021909 (2008).
[25] Y. Han, G.-H. Lu, B.-J. Lee, and F. Liu, Surf. Sci. **602**, 2284 (2008).
[26] S.-C. Li, Y. Han, J.-F. Jia, Q.-K. Xue, and F. Liu, Phys. Rev. B **74**, 195428 (2006).
[27] M. Zinke-Allmang, L. C. Feldman, and M. H. Grabow, Surf. Sci. Rep. **16**, 377 (1992).
[28] K. Morgenstern, Phys. Status Solidi B **242**, 773 (2005).
[29] P. A. Thiel, M. Shen, D.-J. Liu, and J. W. Evans, J. Phys. Chem. C **113**, 5047 (2009).
[30] M. Li, J. W. Evans, C. Z. Wang, M. Hupalo, M. C. Tringides, T.-L. Chan, and K. M. Ho, Surf. Sci. **601**, L140 (2007).
[31] G. Kresse and J. Hafner, Phys. Rev. B **47**, 558 (1993).
[32] J. P. Perdew, K. Burke, and M. Ernzerhof, Phys. Rev. Lett. **77**, 3865 (1996).
[33] G. Kresse and D. Joubert, Phys. Rev. B **59**, 1758 (1999).
[34] G. Henkelman and H. Jónsson, J. Chem. Phys. **113**, 9978 (2000).
[35] M. Prutton, *Introduction to Surface Physics* (Oxford University Press, Oxford, 1987).
[36] D. K. Flynn, W. Wang, S. L. Chang, M. C. Tringides, and P. A. Thiel, Langmuir **4**, 1096 (1988).
[37] H. C. Kang, D. K. Flynn-Sanders, P. A. Thiel, and J. W. Evans, Surf. Sci. **256**, 205 (1991).
[38] J. W. Evans, P. A. Thiel, and M. C. Bartelt, Surf. Sci. Rep. **61**, 1 (2006).
[39] C.-M. Zhang, M. C. Bartelt, J.-M. Wen, C. J. Jenks, J. W. Evans, and P. A. Thiel, Surf. Sci. **406**, 178 (1998).
[40] J. A. Venables, Philos. Mag. **27**, 697 (1973).
[41] M. C. Bartelt and J. W. Evans, Surf. Sci. **298**, 421 (1993).
[42] M. C. Bartelt, L. S. Perkins, and J. W. Evans, Surf. Sci. **344**, L1193 (1995).
[43] Z. Song, J. I. Pascual, H. Conrad, K. Horn, and H.-P. Rust, Appl. Phys. A: Mater. Sci. Process. **72**, S159 (2001).
[44] W. Ho (private communication).
[45] G. A. Eckstein, S. Maupai, A. S. Dakkouri, M. Stratmann, M. Nielsen, M. M. Nielsen, R. Feidenhans'l, J. H. Zeysing, O. Bunk, and R. L. Johnson, Phys. Rev. B **60**, 8321 (1999).
[46] J. P. Pierce, N. C. Bartelt, and K. F. McCarty, Phys. Rev. Lett. **99**, 026101 (2007).
[47] T. M. Wallis, N. Nilius, and W. Ho, Phys. Rev. Lett. **89**, 236802 (2002).
[48] N. Nilius, T. M. Wallis, and W. Ho, Appl. Phys. A: Mater. Sci. Process. **80**, 951 (2005).
[49] C. Chen, C. A. Bobisch, and W. Ho, Science **325**, 981 (2009).
[50] For layer-independent lateral interactions, one finds an aspect ratio for equilibrated bilayer islands of $L_y/L_x \approx (E_{by}+\Delta E_{\mathrm{ads}}/4)/(E_{bx}+\Delta E_{\mathrm{ads}}/4)$ with L_x and L_y measured in atoms. A detailed analysis will be reported elsewhere.

[51] P. A. Thiel, M. Shen, D.-J. Liu, and J. W. Evans, J. Vac. Sci. Technol. A (to be published).
[52] K. Morgenstern, E. Laegsgaard, I. Stensgaard, and F. Besenbacher, Phys. Rev. Lett. **83**, 1613 (1999).
[53] Y. Yao, P. Ebert, M. Li, Z. Zhang, and E. G. Wang, Phys. Rev. B **66**, 041407(R) (2002).
[54] C. A. Jeffrey, E. H. Conrad, R. Feng, M. Hupalo, C. Kim, P. J. Ryan, P. F. Miceli, and M. C. Tringides, Phys. Rev. Lett. **96**, 106105 (2006).